# Generation of multiple attosecond sub-bursts in femtosecond pulse trains by long-wavelength driving lasers

Zhiming Yin, Xiangyu Tang, Xuhong Li, Beiyu Wang, Jiaxin Han, C. D. Lin, and Cheng Jin

Phys. Rev. A **107**, 013114 — Published 25 January 2023

DOI: 10.1103/PhysRevA.107.013114

# Generation of multiple attosecond sub-bursts in femtosecond pulse trains by long-wavelength driving lasers

Zhiming Yin,[1] Xiangyu Tang,[1] Xuhong Li,[1] Beiyu Wang,[1] Jiaxin Han,[1] C. D. Lin,[2] and Cheng Jin[1,3,*]

[1] *Department of Applied Physics, Nanjing University of Science and Technology, Nanjing, Jiangsu 210094, China*
[2] *J. R. Macdonald Laboratory, Department of Physics, Kansas State University, Manhattan, Kansas 66506, USA*
[3] *MIIT Key Laboratory of Semiconductor Microstructure and Quantum Sensing, Nanjing University of Science and Technology, Nanjing, Jiangsu 210094, China*

High-order harmonics generated by a long intense femtosecond laser are known experimentally to create attosecond pulse trains (APTs). In the time domain, an APT consists of a sequence of sharp attosecond bursts that are equally separated by each half optical cycle. Here we show that such well-known features can be modified when longer wavelength driving laser is used. From our simulations, we show that multiple shorter attosecond sub-bursts exist in the femtosecond pulse train within each half optical cycle and the duration of each sub-burst scales approximately as $\lambda_0^{-2}$ with the driving laser wavelength $\lambda_0$. We show that such sub-bursts can be found using quantitative rescattering model for harmonics generated from a single atom and their origin is due to the interference of the quantum orbits from first two returns of the recombining electron. We further show that such sub-bursts can be phase matched under proper laser focusing condition and the position of the gas cell, thus, such new features should be observable experimentally.

## I. INTRODUCTION

High-order harmonic generation (HHG) is a nonlinear optical phenomenon resulting from the interaction of atoms or molecules with an intense femtosecond laser field [1–6]. Due to its unique plateau structure in the spectrum, HHG has been served as coherent light sources in the extreme ultraviolet (XUV) and soft X-rays [7–10]. It has also been used for the generation of attosecond light pulses in the form of attosecond pulse train (APT) [11] and isolated attosecond pulse (IAP) [12] to provide important tools for detecting and controlling ultrafast electronic dynamics inside atoms, molecules, and materials [13–16]. In the development of attosecond light sources, one of the motivations is to reduce its pulse duration to provide better time resolution for probing physical processes. A general scheme for generating attosecond pulses is to spectrally filter the coherent high harmonics. To reduce its duration, extension of harmonics in the plateau region is required according to the uncertainty principle. To date, shortest durations of about 43 as [17] and 53 as [18] have been reported, even though precise characterization of such short pulses remains a contentious issue [19]. These ∼50 as pulses are generated by synthesizing a broad bandwidth (> 100 eV) of soft X-ray (SXR) high harmonics from atoms driven by intense long-wavelength 1.8-$\mu$m lasers. However, further reduction of the duration of attosecond pulses has been hindered by the existence of attochirp of high harmonics [20]. Therefore, it is highly desirable to look for other means to reduce the duration of an attosecond pulse.

It is well known that harmonic emission from a single atom can be well described by a three-step model [21, 22]. In the first step, the electrons are released to the continuum by tunneling ionization; in the second step, the electrons are accelerated in the laser field to obtain higher kinetic energy; in the third step, the electrons recombine with the parent ions and emit high-energy photons, i.e., the high harmonics. For each harmonic order, an electron can follow multiple quantum paths in the continuum [23–34]. According to the excursion time, the first two shortest paths are usually called "short" and "long" orbits (or trajectories). These orbits are for electrons that first return to recombine with the parent ion after strong field ionization. When an electron visits the parent ion more than once, higher-order return orbits can contribute to harmonic generation. We can categorize them by the second return, the third return, and so on, and each return has a "short" and a "long" orbit. There has been continuing interest on the effect of multiple quantum orbits in strong field phenomena. For example, Zaïr *et al.* [31] observed experimentally quantum-path interference between "short" and "long" orbits in the HHG, which could be used to characterize the full single-atom dipole moment. Hickstein *et al.* [30] showed that low-energy features in the measured photoelectron angular distribution are clear signatures giving direct visualization of an electron passing by its parent ion more than once before strongly scattering from it. Petrakis *et al.* [32] experimentally demonstrated a method of spectral control and selection of high harmonics from distinct quantum paths by varying the laser frequency chirp of an intense laser pulse.

For the higher-order returns, since the electron spends more time than one optical cycle, they become more obvious if the driving laser is a multiple-cycle pulse. With long-duration driving laser, it usually results in an APT by spectral filtering high harmonics. Attosecond pulses thus appear in each half optical cycle of driving laser in the APT. When the wavelength of driving laser is in-

* Corresponding author. E-mail: cjin@njust.edu.cn

creased, the spectral region of HHG is greatly extended since the photon energy of harmonic cutoff is scaled as $\lambda_0^2$, where $\lambda_0$ is the laser wavelength. This condition becomes a prerequisite for reducing the duration of attosecond pulse in the APT. On the other hand, the effects of higher-order returns are more evidently manifested in the HHG process when the driving laser has a long wavelength. For example, Hernández-García *et al.* [25] reported a route to generate zeptosecond waveform structure in the temporal pulse of X-ray high harmonics by controlling the duration and carrier-envelope offset of >7 μm driving laser pulses, which is due to the interference of X-ray emissions from multiple scattering events. In a later theoretical work, He *et al.* [24] showed that the weight of the contribution from the electron's higher-order returns to the HHG increases with the laser wavelength. With the development of laser technology in optical parametric amplification (OPA) and optical parametric chirped pulse amplification (OPCPA), long-wavelength MIR lasers become largely available in the labs [7, 35, 36]. It is thus of great interest to explore the possibility of generating sub-bursts inside each pulse train by taking advantage of ascending contribution from higher-order quantum orbits with long-wavelength MIR driving lasers.

To fully describe the generation of HHG, or the attosecond pulse, one also needs to consider the propagation effect of high harmonics in a macroscopic nonlinear medium [37–39]. Efficient generation of HHG is mainly determined by good phase matching between the geometric phase of the focused driving laser and the induced-dipole phase accumulated due to the motion of the electron in the continuum. The later phase is approximately proportional to the laser intensity and becomes larger for the higher-order return quantum orbit as the electron spends more time in the continuum [40]. Thus phase-matching conditions are quite different for high harmonics due to different quantum orbits. Since high harmonics caused by higher-order return quantum orbits have relatively large phases, they are generally difficult to phase match in the gas medium. The meaningful control of the duration of attosecond pulse by selecting high harmonics from higher-order returns obtained from single-atom theory should be examined by including propagation effect. This has been rarely performed previously.

In this work, our main goal is twofold. First, we will demonstrate that contribution of higher-order returns to HHG driven by the MIR lasers can be utilized to produce attosecond sub-bursts in the femtosecond pulse train (FPT) at the level of single-atom response. Such pulse train occurs in every half optical cycle. Second, we will calculate the HHG phase due to higher-order return orbits and will search condition for good phase matching. This paper is arranged as the following. In Sec. II, we will give the theoretical methods for simulating single-atom HHG, the macroscopic propagation in the gas medium, and the far-field harmonic emissions. In Sec. III, we will first discuss the generation of attosecond sub-bursts due to the interference of high harmonics from the first and second return orbits using long-wavelength MIR driving lasers at the single-atom response. We will then calculate the phases for different quantum orbits, which are then used to analyze phase-matching conditions (or the spatial map of coherence length) of HHG. We will finally show the results of attosecond pulses in the far field after macroscopic propagation under the favorable conditions. The conclusions will be given in Sec. IV.

## II. THEORETICAL METHODS

### A. Theory of single-atom HHG response

To simulate the response of a single atom under an ultrafast intense laser pulse, the most accurate way is to numerically solve the time-dependent Schrödinger equation (TDSE). However, this approach is quite time consuming and the physics of electron dynamics is not easy to uncover. Alternatively, a model based on the strong-field approximation (SFA) proposed by Lewenstein *et al.* [41] has been widely applied for simulating single-atom HHG. A quantum orbital (QO) model [42–46] has been further established by applying the saddle-point approximation to separate harmonic emissions from different quantum paths. To overcome the drawback of the SFA, a quantitative rescattering (QRS) model [46–48] has been developed in which the interaction of the returning electron and the ionic core has been properly treated. The QRS model has been confirmed by comparing with those from solving three-dimensional TDSE and with many experiments, see Ref. [49].

#### 1. *Quantitative rescattering (QRS) model*

In the QRS model [46–48], the induced-dipole moment of an atomic target under a linearly polarized laser can be written as:

$$x(\omega) = W(\omega)d(\omega), \tag{1}$$

where $d(\omega)$ is the complex photorecombination (PR) transition dipole matrix element, which reflects the properties of the target, and $W(\omega)$ is the complex microscopic wave packet, which is mostly determined by the laser and the ionization potential of the target.

In the QRS model, $d(\omega)$ can be precisely calculated by solving the time-independent Schrödinger equation under the single-active electron (SAE) approximation, in which the interaction between the electron and the atomic ion is described by a model potential [50]. $d^{SFA}(\omega)$ in the Lewenstein (or SFA) model is obtained by assuming that the continuum state of the ionized electron is a plane wave, which is not accurate. Meanwhile the wave packet W($\omega$) in the QRS model is the same as that in the SFA model, and it can be calculated using the Lewenstein

model or the quantum orbit model:

$$W(\omega) = \frac{x^{SFA}(\omega)}{d^{SFA}(\omega)}, \tag{2}$$

or

$$W(\omega) = \frac{x^{QO}(\omega)}{d^{SFA}(\omega)}. \tag{3}$$

Here $x^{SFA}(\omega)$ and $x^{QO}(\omega)$ are complex induced-dipole moments, and $d^{SFA}(\omega)$ is a pure imaginary or a pure real number.

### 2. *Lewenstein (or SFA) model*

According to the Lewenstein model under the strong-field approximation (SFA) [41], the time-dependent induced dipole moment can be written in the form of the following integral,

$$\begin{aligned} x(t) = &- i\int_{-\infty}^{t} dt' \left(\frac{-2\pi i}{t-t'-i\epsilon}\right)^{3/2} d_x^*\left(p_s + A(t)\right) \\ &\times d_x\left(p_s + A\left(t'\right)\right) E\left(t'\right) e^{-iS\left(p_s,t,t'\right)} + c.c., \end{aligned} \tag{4}$$

where $E(t)$ is the applied laser field, $A(t)$ is the vector potential, $p_s$ is the saddle-point solution for momentum, which is given by

$$p_s = -\frac{1}{t-t'}\int_{t'}^{t} A(t'')dt'', \tag{5}$$

and $S(p_s, t, t')$ is the classical action of the electron during propagation in the electric field, which is expressed as

$$S(p_s, t, t') = \int_{t'}^{t} dt''(\frac{1}{2}[p_s + A(t'')]^2 + I_p), \tag{6}$$

where $I_p$ is the ionization potential of the target, and $t'$ and $t$ are the ionization and recombination moments of the electron, respectively. Note that in Eq. (4), one can truncate the excursion time of the electron to select contribution to the single-atom HHG (or the electron wave packet) from different returns.

For hydrogenlike atoms, the dipole matrix element describing the transition from the ground state to the continuum is given by

$$d(p) = \langle p|\hat{d}|g\rangle = i(\frac{2^{7/2}(2I_p)^{5/4}}{\pi})\frac{p}{(p^2+2I_p)^3}. \tag{7}$$

### 3. *Quantum orbit (QO) model*

Applying the saddle-point approximation, the following two equations can be obtained for the harmonic with angular frequency $\omega$ [42–46]:

$$\frac{1}{2}[p_s + A(t')]^2 = -I_p, \tag{8}$$

and

$$\frac{1}{2}[p_s + A(t)]^2 = \omega - I_p. \tag{9}$$

Here the first equation corresponds to the quantum effect of tunneling ionization of the electron, and the second equation represents the energy of the photon ($\omega$) emitted by the recombination of the electron and the parent ion.

The induced-dipole moment in the frequency domain can be expressed as:

$$\begin{aligned} x(\omega) = &\sum_s \frac{2\pi}{\sqrt{\det\left(S''\right)}}\left(\frac{-2\pi i}{t_s - t_s'}\right)^{3/2} d_x^*\left(p_s + A\left(t_s\right)\right) \\ &\times d_x\left(p_s + A\left(t_s'\right)\right) E\left(t_s'\right) e^{-i\Theta\left(p_s,t_s,t_s'\right)}, \end{aligned} \tag{10}$$

where each pair $(t_s, t_s^{'})$ determines a unique quantum orbit represented by $s$, the phase factor $\Theta(p_s, t, t^{'}) = S(p_s, t, t^{'}) - \omega t$, and the calculation of the determinant $\det(S'')$ is straightforward. In Eq. (10), one can select the contribution to the single-atom HHG (or the electron wave packet) either from one specific quantum orbit or from multiple quantum orbits.

## B. Propagation equations of the high-harmonic field

We assume that the laser beam is not affected when it propagates in a macroscopic gas medium. By employing a moving coordinate frame ($z' = z$ and $t' = t - z/c$) and applying the paraxial approximation, the Maxwell's wave equations for high-harmonic field in the frequency domain are [51–54]

$$\begin{aligned} &\nabla_\perp^2 \tilde{E}_h\left(\mathrm{r}, z', \omega\right) - \frac{2i\omega}{c}\frac{\partial \tilde{E}_h\left(\mathrm{r}, z', \omega\right)}{\partial z'} \\ &\quad = -\mu_0\omega^2 \tilde{P}_{nl}\left(\mathrm{r}, z', \omega\right) \end{aligned} \tag{11}$$

where

$$\tilde{E}_h(r, z', \omega) = \hat{F}[E_h(r, z', t')], \tag{12}$$

$$\tilde{P}_{nl}(r, z', \omega) = \hat{F}[P_{nl}(r, z', t')], \tag{13}$$

and

$$P_{nl}(r, z', t') = n_0 x(r, z', t'). \tag{14}$$

Here $\hat{F}$ is the Fourier transform operator acting on the temporal coordinate, $P_{nl}(r, z', t')$ is the nonlinear polarization defined in Eq. (14), and $n_0$ is the neutral atom density. $x(r, z', t')$ is the induced-dipole moment in the time domain obtained with a local laser field at the spatial position $(r, z')$, and it can be related to $x(\omega)$ in Eq. (1) by an inverse Fourier transform. Once Eq. (11) is solved, the harmonic field $\tilde{E}_h(r, z', \omega)$ at the exit face of the gas medium is called the near-field harmonic.

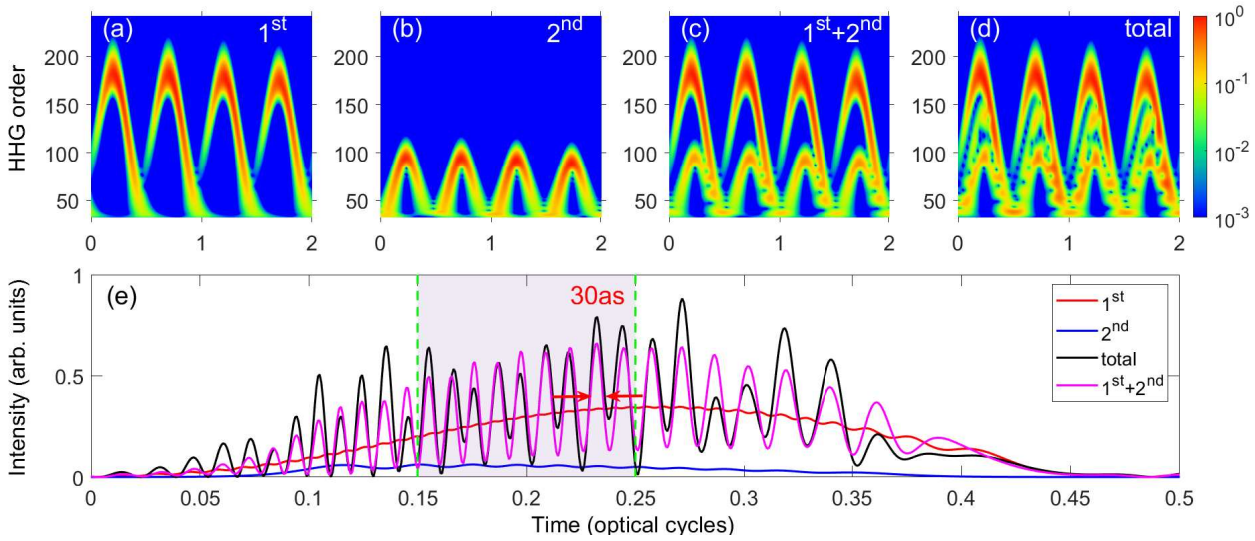


FIG. 1. Time-frequency analysis of single-atom harmonic emission due to first-return orbits (a), the second-return orbits (b), and the orbits of both returns (c). The results for including all orbits are in (d). Note that the values in (a)-(d) are normalized individually. (e) Temporal profiles of the attosecond pulses synthesized from single-atom high harmonics from different orbits in (a)-(d). The width of the attosecond sub-burst is 30 as due to the interference of quantum orbits from the first and second returns. Here the 1600-nm laser has the intensity of $1.5 \times 10^{14}$ W/cm$^2$ and the total pulse duration is 30 cycles. The QRS model is applied, in which the microscopic wave packet is computed by truncating the electron excursion time in the standard SFA model to select contributions from a specific return.

### C. Far-field harmonic emission

The propagation of high-harmonic field in a gas medium can be simulated rigorously by solving the Maxwell's wave equations. Its propagation in the vacuum can be carried out using Huygens integral under the paraxial and Fresnel approximations. The harmonic in the far field is obtained by the near-field harmonic by

$$E_h^f(r_f, z_f, \omega) = ik \int \frac{\tilde{E}_h(r, z', \omega)}{z_f - z'} J_0\left(\frac{krr_f}{z_f - z'}\right) \exp\left[-\frac{ik\left(r^2 + r_f^2\right)}{2(z_f - z')}\right] \times r dr, \tag{15}$$

where $J_0$ is the zero-order Bessel function of the first kind, $z_f$ and $z$ are the far-field and near-field position from the laser focus, $r_f$ is the transverse coordinate in the far field.

## III. RESULTS AND DISCUSSION

### A. Generation of attosecond sub-bursts in the pulse train by the interference of quantum orbits

We first calculate HHG and attosecond pulses at the level of single-atom response. In the calculation, the electric field of the laser pulse takes the form

$$E(t) = E_0 \cos^2\left(\frac{\pi t}{\tau}\right) \cos(\omega t + \varphi). \tag{16}$$

Here $\tau$ is the total duration, which is 2.75 times the full-width-at-half-maximum (FWHM) duration of the laser pulse, $\varphi$ is the carrier-envelope-phase (CEP), and $E_0$ is the peak strength. The target is neon atom. The laser peak intensity is $1.5 \times 10^{14}$ W/cm$^2$, the total duration is 30 optical cycles, and the CEP is fixed at 0. With the QRS model, the simulated HHG and attosecond pulses are shown in Fig. 1 using a driving laser with wavelength of 1600 nm. The time-frequency analysis of high harmonics due to quantum orbits from the first return is shown in Fig. 1(a), and for the second return in Fig. 1(b). In Figs. 1(c) and (d), quantum orbits from the first and second returns, and from all returns are included, respectively. Here, contribution from a specific return is selected by truncating the electron excursion time in the SFA model. One can see that the first and second returns give quite different harmonic cutoffs, see Figs. 1(a) and (b). Harmonic emissions due to these two returns are well resolved even after all quantum paths have been included, see Figs. 1(c) and (d). We synthesize high harmonics with photon energies above $0.3U_p + I_p$, where $U_p$ is the pondermotive energy of the electron. The intensity of the resulting attosecond pulses can be explicitly calculated as

$$I_{APTs}(t) = \left| \int_{\omega'}^{\infty} \omega^2 x(\omega) e^{i\omega t} d\omega \right|^2, \tag{17}$$

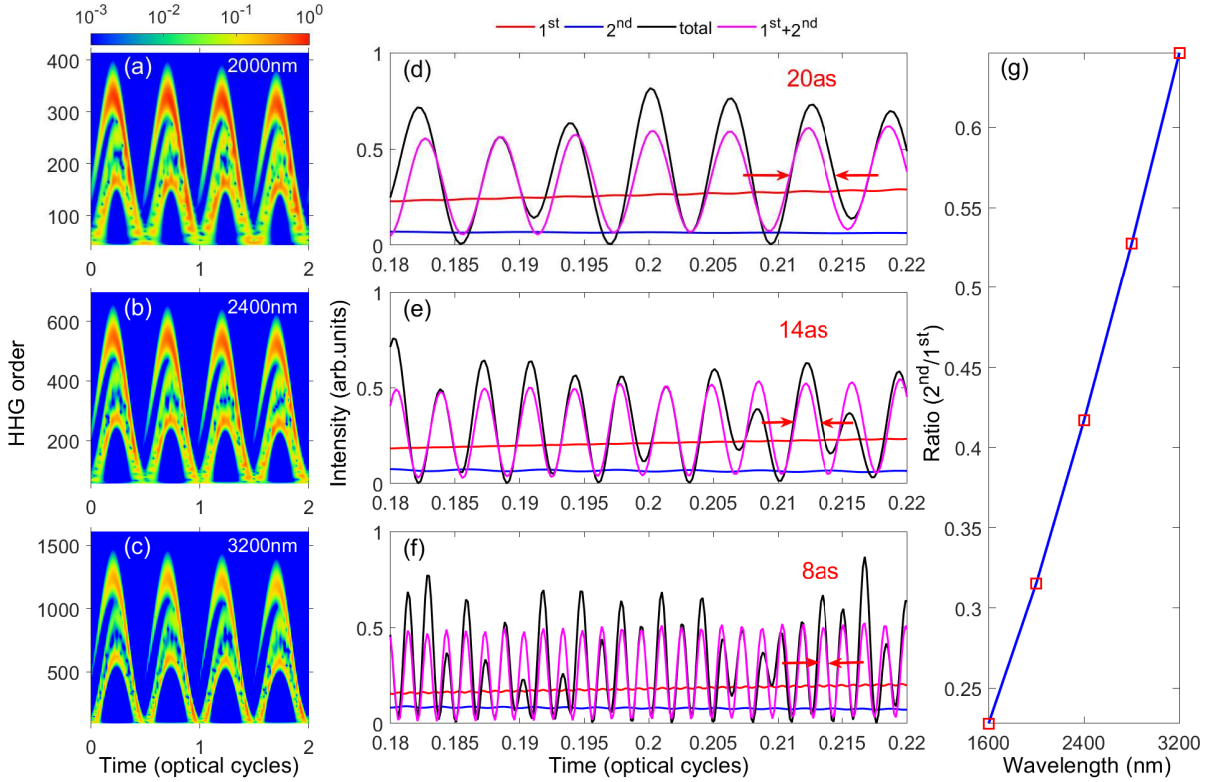


FIG. 2. Time-frequency analysis of single atom HHG driven by lasers with wavelengths of 2000 nm (a), 2400 nm (b), and 3200 nm (c). The intensity and number of cycles of the total duration are kept the same as those in Fig. 1. (d)-(f): Temporal profiles of attosecond pulses by spectral filtering high harmonics from different quantum orbits at different wavelengths as indicated. The widths of attosecond sub-bursts due to the interference of the first and second return orbits are 20 as, 14 as, and 8 as at the three different driving wavelengths, respectively. (g) The intensity ratio of HHG due to the second return and first return orbits as a function of the wavelength.

where $\omega' = (0.3U_p + I_p)/\hbar$. And the results are shown in Fig. 1(e). Including quantum orbits from individual first or second return, a single pulse (red or blue line) occurs within each half optical cycle of the driving laser. By considering the interference of quantum paths from both first and second returns, multiple fine oscillatory temporal structures (purple line) with FWHM width of about 30 as over each half optical cycle appear. The strength of such temporal structures (to be called "attosecond sub-bursts" from here on) are slightly modified (black line) if higher returns (more than two) are added, but the number and the width of attosecond sub-burst is not changed.

The attosecond sub-bursts appearing in the time interval of electron recombination, i.e., about half optical cycle, can be interpreted quantitatively. For simplicity, we only consider the interference of two harmonic cutoffs generated by the first and second returns. The period of an attosecond sub-burst is given by

$$T_1 = \frac{2\pi}{\omega_1 - \omega_2} = \frac{2\pi\hbar}{(3.17U_p + I_p) - (1.54U_p + I_p)} = \frac{2\pi\hbar}{1.63U_p}. \quad (18)$$

Note that the central photon energy of the synthesized pulse train can be estimated as $1.735U_p + I_p$, thus the corresponding period is about twice of the FWHM duration of the attosecond sub-burst according to Eq. (18). Here $\omega_1$ and $\omega_2$ represent the angular frequencies of the two harmonic cutoffs with $3.17U_p$ and $1.54U_p$ being the maximum electron kinetic energies from first and second returns, respectively. $T_1/2$ is approximately the FWHM of the attosecond sub-burst, which is calculated to be 35 as with $U_p = 35.85$ eV by using the given laser parameters. The number of attosecond sub-bursts in the time range from 0.15 to 0.25 cycles [grey area in Fig. 1(e)] can be calculated as

$$n = [\frac{0.1T_0}{T_1}] = [\frac{0.2\pi}{\omega_0 T_1}], \quad (19)$$

where $T_0$ and $\omega_0$ are the period and the angular frequency of the driving laser, respectively. The calculated number $n$ is 8 ($n$ is rounded up to an integer). Both the number of attosecond sub-bursts and the width of each calculated one from simple formulas agree very well with those shown in Fig. 1(e). We have also checked that the depletion of the ground state can be neglected when forming the attosecond sub-burst structure.

We next calculate attosecond sub-bursts by increasing the wavelength of the driving laser, with fixed peak laser intensity and fixed number of optical cycles. Time-frequency analysis of high harmonics are shown in Figs. 2(a)-(c) for the driving wavelengths of 2000 nm, 2400 nm, and 3200 nm, respectively. In the calculations, the quantum orbits from all returns are included. Interference of harmonic emissions from quantum orbits of first and second returns can be clearly seen. By spectral filtering the high harmonics, the temporal pulses are plotted (black lines) in Figs. 2(d)-(f). One can see that as laser wavelength is increased, the number of attosecond sub-bursts is increased in the fixed time range measured by the optical cycles, while its FWHM duration is scaled approximately as $\lambda_0^{-2}$ as indicated in the figure, where $\lambda_0$ is the wavelength of the driving laser. The structure of the attosecond sub-burst is caused mostly by the interference of high harmonics due to quantum orbits of first and second returns, see purple lines in Figs. 2(d)-(f).

We also check the intensity ratio of high harmonics due to the second and first returns. This ratio is defined to be the integrated harmonic intensity due to the second return from $0.3U_p + I_p$ to $1.6U_p + I_p$ with respect to first return from $2.0U_p + I_p$ to $3.2U_p + I_p$. Fig. 2(g) shows the intensity ratio as the laser wavelength is increased, meaning the importance of second return increases with wavelength in comparison to first return. This conclusion is consistent with what has been found in He *et al.* [24] that the yield weight of harmonics generated by higher-order return orbits increases with the wavelength. Therefore, one can expect that interference effect in attosecond sub-bursts due to the first and second return orbits becomes more important with the increase of laser wavelength.

To verify the accuracy of the QRS model employed in the above calculations, we simulate the single-atom HHG by using the TDSE method. Comparison of time-frequency analysis of harmonic emissions from the QRS model and the TDSE method are shown in Figs. 3(a) and (b). Harmonic emissions from first, second, and higher returns from the two calculations clearly agree with each other quite well, including the trajectory structures and the relative strengths of harmonic emissions from different returns. We further show the temporal attosecond sub-bursts in Fig. 3(c), where the number of attosecond sub-bursts and the width are also in good agreement. Thus, the QRS model can be used to correctly predict the behaviors of quantum orbits in the HHG process driven by MIR lasers. Note that Hernández-García *et al.* [25] have theoretically predicted similar sub-bursts with zeptoseconds duration using a longer wavelength of 3.9-$\mu$m laser. Their calculation was performed using the SFA+ approach [55]. They attributed such sub-burst structure to the interference of X-ray harmonic emissions from multiple quantum orbits, including first-return, second-return, and third return orbits. However, we have identified that harmonic emissions from third-return orbits are very weak for the wavelength of the driving laser we considered.

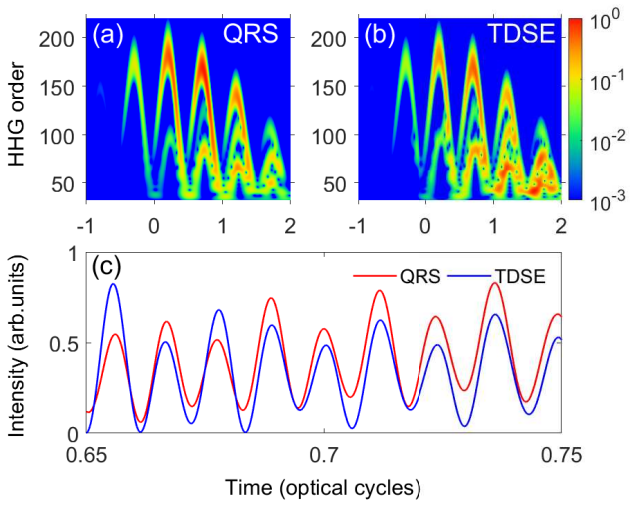


FIG. 3. Time-frequency analysis of single-atom HHG obtained from the QRS model (a) and from the TDSE method (b). (c) Temporal profiles of attosecond sub-bursts by spectral filtering high harmonics in (a) and (b). The laser parameters are the same as those in Fig. 1 except that the FWHM duration is 3 optical cycles.

## B. Phase-matching analysis of HHG from different quantum orbits

### 1. *Induce-dipole phase*

In this section we examine whether the attosecond sub-burst waveforms in the pulse train identified in single atom response can be realized in actual experiments. For this purpose, we first analyze phase-matching conditions for high harmonics from each of multiple quantum orbits upon propagation in a gas medium. In quantum orbit theory, the phase of the induced dipole is larger the longer the quantum orbit in the continuum is, which in turn makes phase matching more difficult and the far-field harmonics emitted at a greater divergence angle [46, 56–59]. The induced-dipole phase can be calculated in the frame of the SFA by using the classical trajectory of the electron under the external electric field as [40, 60, 61]

$$\varphi_i(p_s, t, t') = S(p_s, t, t') - q\omega_0 t, \tag{20}$$

where $i = S1$, $L1$, $S2$, $L2$, $S3$, $L3$, ..., standing for different quantum orbits, and $t'$ and $t$ are the electron ionization and recombination times obtained by solving the Newton's equation of motion, respectively. Here, "S1" refers to the short quantum orbit in the first return, "L1" the long quantum orbit in the first return and so forth. In Fig. 4(a), the induced-dipole phase of harmonic order 23 (H23) as a function of laser peak intensity is shown

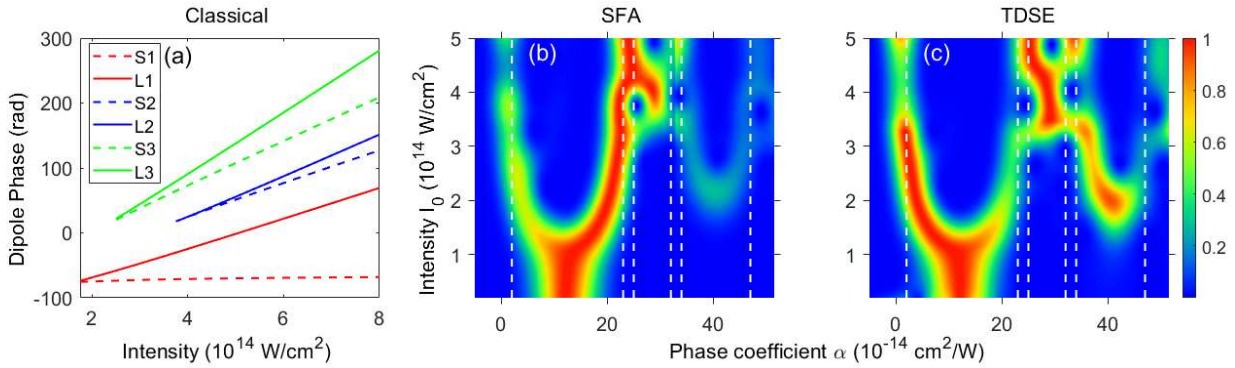


FIG. 4. (a) Induced dipole phase as a function of laser intensity for different quantum orbits (indicated by "S1", "L1", ...) calculated using classical trajectories. The distributions of quantum orbits characterized by the laser intensity $I_0$ and the phase coefficient $\alpha$ simulated by the SFA theory (b) and by the TDSE method (c). Note that the QRS model gives the same distribution of quantum orbits as the SFA model at a given harmonic order. The wavelength of the driving laser is 800 nm and the harmonic order is H23.

for the first six quantum orbits at 800 nm. The phase depends linearly on the laser intensity, and can be written as

$$\varphi_i = \alpha_{i,q} \cdot I. \tag{21}$$

Here $\alpha_{i,q}$ is the phase coefficient for $q$-th harmonic order and $I$ is the laser intensity. The values of $\alpha_{i,q}$ extracted from Fig. 4(a) are listed in Table I.

TABLE I. According to the classical model, the calculated $\alpha$ coefficients of each orbits at 800 nm, 1200 nm, 1600 nm, and 2000 nm. Here the unit of the $\alpha$ coefficient is rad $\cdot$ W$^{-1}cm^2$.

| $\lambda_0$(Hq) | $\alpha_{S1}$ | $\alpha_{L1}$ | $\alpha_{S2}$ | $\alpha_{L2}$ | $\alpha_{S3}$ | $\alpha_{L3}$ |
|---|---|---|---|---|---|---|
| 800 nm (H23) | 1.5 | 23.5 | 25 | 32 | 34 | 48 |
| 1200 nm (H83) | 5 | 80 | 84 | 109 | 113 | 162 |
| 1600 nm (H175) | 12 | 190 | 199 | 259 | 268 | 383 |
| 2000 nm (H321) | 26 | 370 | 388 | 506 | 526 | 748 |

The phase coefficient $\alpha_{i,q}$ also can be extracted from the intensity-dependent induced-dipole moments calculated by the SFA (or QRS) model and the TDSE method. The contribution from the phase component $\alpha_{i,q}$ over a range of intensities close to $I_0$ can be expressed as follows [62–66]:

$$D_q(\alpha_{i,q}, I_0) = \int x_q(I) \exp(i\alpha_{i,q} I) G(I - I_0) dI, \tag{22}$$

where $x_q(I)$ represents the induced-dipole moment of the $q$-th harmonic, and $G(x) = e^{-x^2/(4a)}$ is the Gaussian window function with an adjusted parameter $a$. By employing the trapezoidal pulse shape for the driving laser, the quantum path distributions in terms of $\alpha_{i,q}$ and $I_0$ are simulated by the SFA model and the TDSE method in Figs. 4(b) and (c), respectively. The values of $\alpha_{i,q}$ for different quantum orbits are indicated (white dashed lines) in these figures. It can be seen that for laser intensities generating H23 in the plateau, the $\alpha_{i,q}$ from classical trajectories are in a general agreement with the distributions of quantum paths for both the SFA and TDSE results. The quantum-path distributions simulated by the SFA model are plotted for the laser wavelengths of 1200 nm, 1600 nm, and 2000 nm in Figs. 5(a)-(c), respectively. The selected harmonic orders are labeled in these figures. Note that the coefficients $\alpha_{i,q}$ do not depend much on the harmonic order. The white lines are the extracted coefficients $\alpha_{i,q}$ from the induced-dipole phases by the classical trajectories as shown in Figs. 5(d)-(f). These values are also listed in Table I. With the increase of laser wavelength, the orbital feature in the distribution of $|D_q(\alpha_{i,q}, I_0)|^2$ becomes more obvious. The general agreement between the distribution of quantum orbit and the classical value of $\alpha_{i,q}$ is also achieved. In addition, from Table I, for a given quantum orbit, the coefficient $\alpha$ approximately scales as $\lambda_0^3$.

### 2. *Coherence length of HHG for different quantum orbits*

For phase matching of HHG, we consider effect caused by the geometric phase of the driving laser beam and the the intrinsic induced-dipole phase accumulated by the electron following the specific quantum orbit. For our purpose here we ignore contributions from the neutral atom dispersion and the plasma defocusing. This model is valid when the gas pressure is low and the laser intensity is low.

The phase mismatch of wave vectors between the $q$th harmonic and the fundamental driving laser can be expressed as [51, 52, 67, 68]:

$$\delta k_q(r, z) = k_q - |q\mathbf{k}_1 + \mathbf{K}|, \tag{23}$$

where $k_q = q\omega_0/c$, $\mathbf{k}_1$ is the total wave vector of the driving laser and $\mathbf{K}$ is the effective wave vector of single-

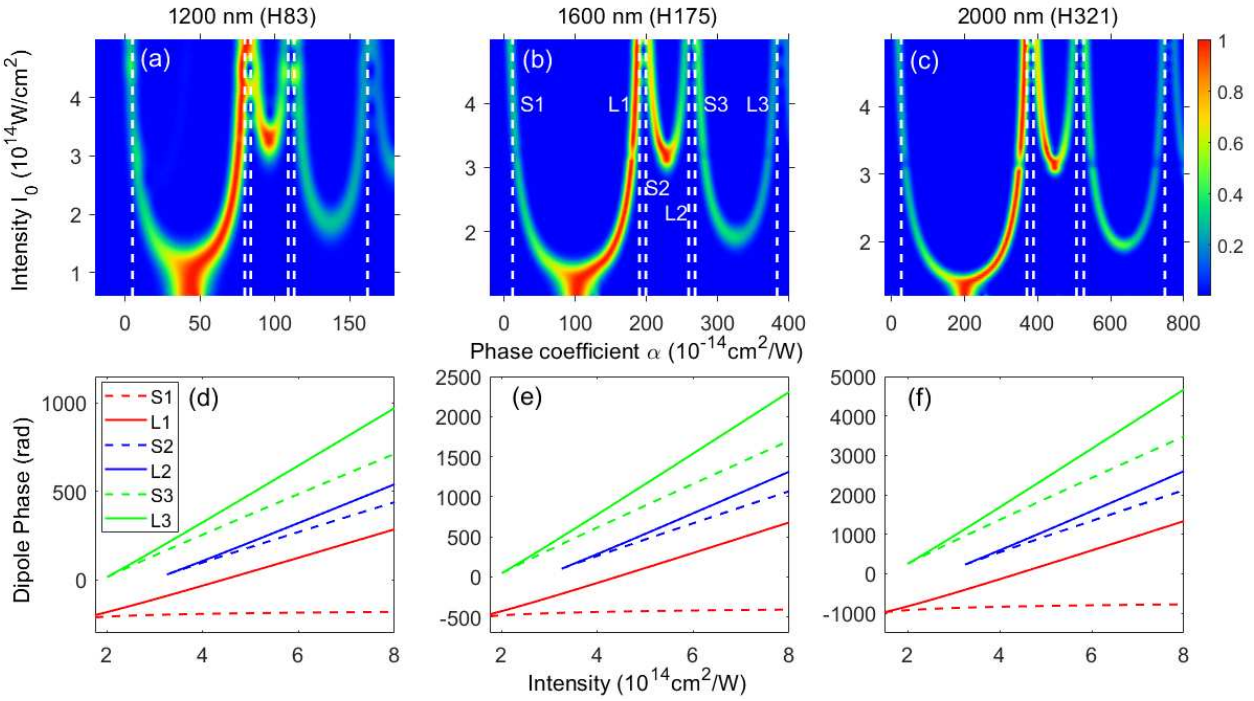


FIG. 5. Distributions of quantum orbits simulated by the SFA model at the laser wavelengths of 1200 nm (a), 1600 nm (b), and 2000 nm (c) for the selected harmonic orders. The corresponding induced dipole phases calculated by the classical trajectory for different quantum orbits are shown in (d)-(f).

atom response. $\mathbf{k}_1$ is explicitly expressed as

$$\mathbf{k}_1(r,z) = k_0\mathbf{e}_z - \nabla\varphi(r,\phi,z), \tag{24}$$

where $\mathbf{e}_z$ is the unit vector along the $z$ direction, $\varphi(r,z)$ is the geometric phase of the driving light, and $k_0 = \omega_0/c$. The wave vector $\mathbf{K}$ describing the spatial dependence of the atomic phase is given by

$$\mathbf{K}(r,z) = \nabla\varphi_{q,dip}(r,z). \tag{25}$$

Here $\varphi_{q,dip}(r,z)$ is the intrinsic induced-dipole phase accumulated by an electron moving along a given quantum orbit in the laser field. Its dependence on the laser intensity is written as

$$\varphi_{q,dip}(r,z) = -\alpha_{i,q}I(r,z), \tag{26}$$

where $I(r,z)$ is the spatial peak intensity of the driving laser.

Finally, the coherence length of HHG can be defined as

$$L_{q,coh}(r,z) = \frac{\pi}{|\delta k_q(r,z)|}. \tag{27}$$

The phase-matching conditions of HHG can be optimized by varying the macroscopic parameters. Below we will show two examples to demonstrate that good phase-matching conditions for HHG due to high-order return quantum orbits can be achieved. We first simulate the coherence length of high harmonics generated by a 1600-nm driving laser, see Fig. 6. The laser beam is assumed Gaussian, its beam waist at the focus is $w_0 = 130$ $\mu$m, and peak intensity at the focus is $1.5 \times 10^{14}$ W/cm$^2$. In Fig. 6, the spatial distributions of coherence length by "short" orbits are shown on the left column and by "long" orbits are shown on the right column, for the first three returns, respectively. The direction of the arrow in the figure gives the direction of the wave vector of the harmonic, determining its divergence in the far field. What we are interested in here is to selectively maintain the contributions to the HHG from quantum orbits other than the S1, i.e., the "short" orbit in the first return. This can be achieved by varying the position of a gas target relative to the laser focus since the size of a gas jet is usually much shorter than the Rayleigh range of the driving laser. For all quantum orbits other than the S1, a narrow good phase-matching region (white strip) starting from the off-axis position before the laser focus and continuing until near the laser focus and close to the axis is observed. Because only in the white strip region phase mismatch caused by the induced-dipole phase of long quantum orbits can be mostly compensated by that due to the geometric phase of the driving laser. On the other hand, the direction of harmonic wave vector is quite different before laser focus for different long quantum orbits. If the gas medium is put before the laser focus, the harmonics from different quantum orbits cannot in-

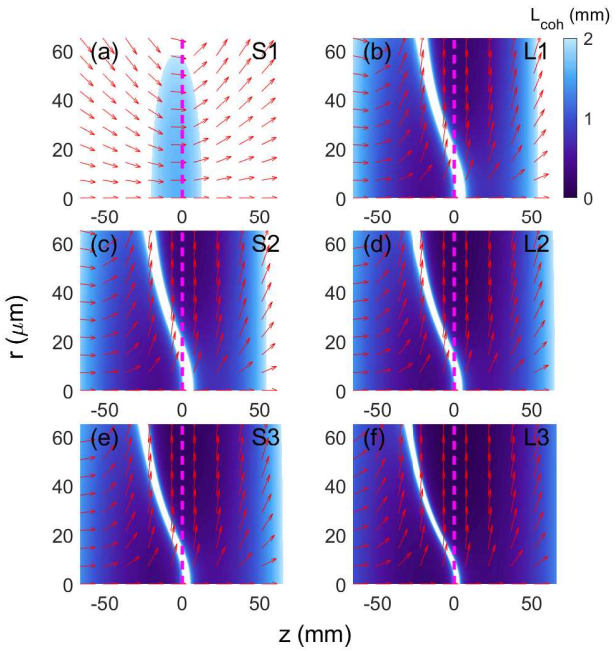


FIG. 6. Map of coherence length of harmonic H65 generated by different quantum orbits. From top to bottom row, the first, second, and third returns are plotted. The left column are for "short" orbits, and the right column are for "long" ones. The red arrow indicates the direction of the harmonic wave vector. The peak intensity and the beam waist at the focus of the 1600-nm Gaussian beam are $1.5 \times 10^{14}$ W/cm$^2$ and 130 $\mu$m, respectively.

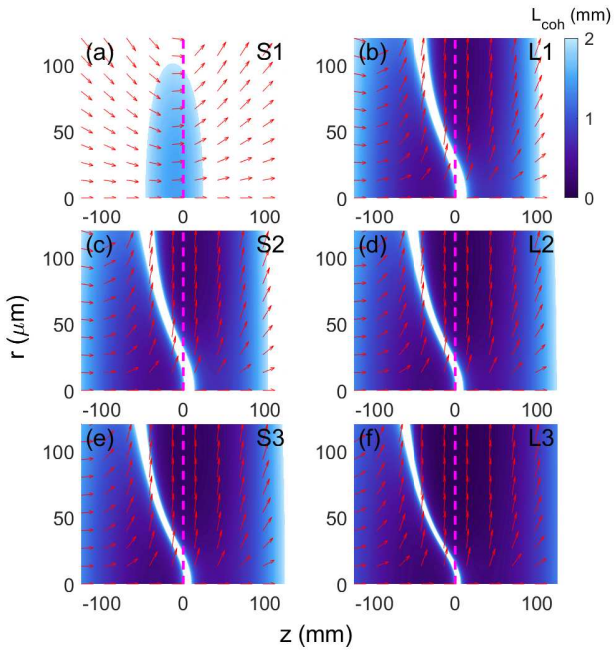


FIG. 7. Same as Fig. 6 but for a 2000-nm driving laser with a beam waist of 200 $\mu$m and a harmonic order of 131.

terfere coherently because they have different divergence angles. Thus, one would choose to put the gas medium at the focus to minimize the diverging effects of HHG from different quantum orbits.

Similarly, we carry out similar simulations using a 2000-nm driving laser, see Fig. 7. To improve phase matching of quantum orbits with longer wavelength, a more loosely focused beam is required. The beam waist of the driving laser is thus set to 200 $\mu$m, with the same peak intensity. The behaviors of coherence lengths are very similar to Fig. 6, so the gas should be placed also at the laser focus. Note that the evolution of high-harmonic field in a gas medium is reflected in the coherence length map, which has been demonstrated in our previous works [51, 52]. With the guidance of the coherence lengths in Figs. 6 and 7, we will next show the results of HHG and attosecond pulses by performing numerical simulations by solving the Maxwell's wave equations of the high-harmonic field.

### C. Macroscopic HHG and attosecond pulses after propagation in the gas medium

#### 1. *HHG in the far field*

With the macroscopic parameters used in Fig. 6, we simulate the HHG in Fig. 8 by setting the center of a 1-mm long gas jet at the laser focus. In the simulations, we first solve the Maxwell's wave equations of the high-harmonic field in the gas medium, and then obtain the spatial distributions of HHG in the far field by using Huygens integration. The single-atom induced dipoles are calculated by the QRS model with the separation of quantum paths in the frame of quantum orbits model. Fig. 8(a) gives the intensity distribution of far-field high harmonics by including all quantum paths. Figs. 8(b)-(d) show the intensity profiles due to the "short" orbits, S1, S2, S3, respectively, and the results for the "long" orbits L1, L2, L3 are plotted in Figs. 8(f)-(h). One can see that only the harmonics generated from S1 have small divergence, while all the other orbits result in similar and larger divergence in the far field. For the L1 shown in Fig. 8(f), the spectrum is wider when the divergence angle is small, and becomes narrower when the divergence angle is increased. Fig. 8(e) gives the integrated HHG spectra over the divergence angle by quantum orbits from three different returns separately. One can see that at the desired macroscopic conditions the harmonic yields of the second-return orbits after propagation can be comparable to that of the first-return ones, which provides the prerequisite for the conspicuous interference between

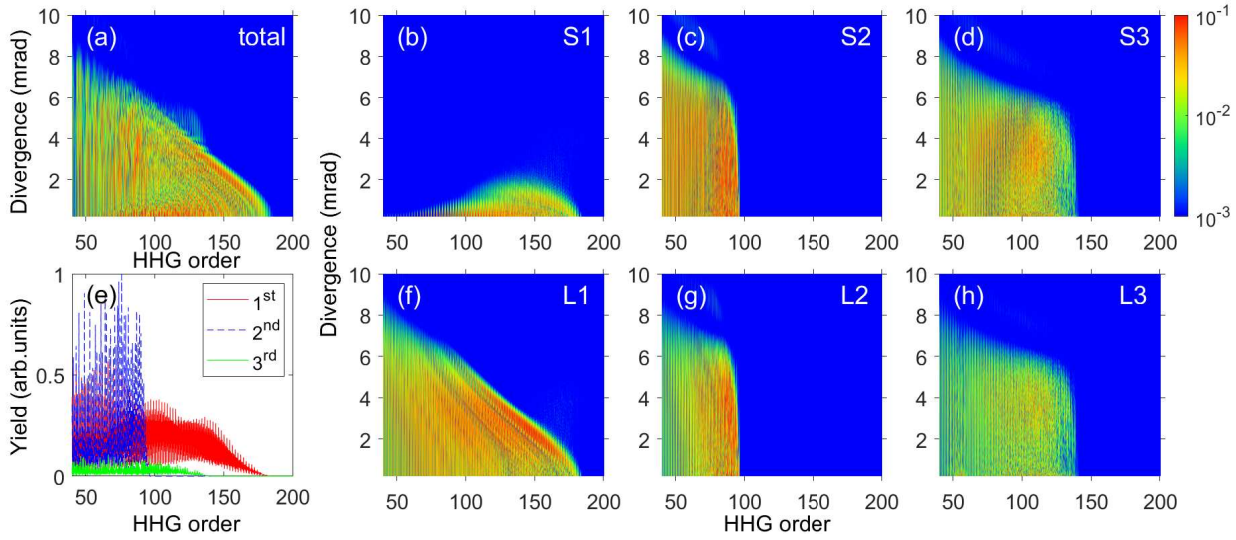


FIG. 8. (a) Intensity distribution of the macroscopic HHG in the far field generated by including all quantum orbits. Intensity distributions of the far-field HHG generated by individual "short" orbits from the first three returns are shown in (b)-(d), and those results by individual "long" orbits are plotted in (f)-(h). (e) HHG spectra by integrating the harmonic yield over the divergence angle are shown for quantum orbits from different returns. The driving laser has a wavelength of 1600 nm, other laser and macroscopic parameters can be seen in the text.

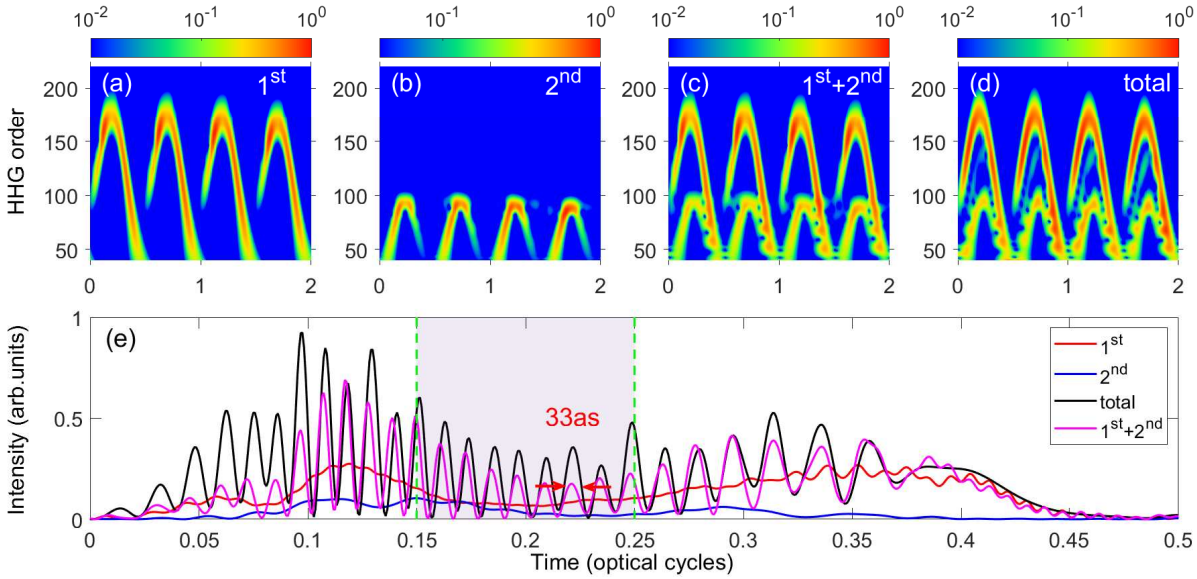


FIG. 9. Similar figure to Fig. 1 but for the macroscopic HHG at 1 mrad in the far field.

quantum orbits. Meanwhile the harmonic yields of the third-return orbits are relatively low, so they do not have considerable contribution to the total harmonic yields after macroscopic propagation. Note that the sensitive dependence of the phase-matching condition on the location of the gas medium has been intensely discussed [69, 70], and it has been known that the good phase matching for the "long" orbits in the first return can be achieved when the gas medium is located at the laser focus [42].

### 2. *Macroscopic attosecond sub-bursts*

We choose a divergence angle of 1 mrad to analyze the temporal structure of attosecond sub-bursts synthesized by the macroscopic HHG in Fig. 8. The time-frequency analysis of the high-harmonic field generated by the quantum orbits from separated first and second returns, and by both return orbits are shown in Figs. 9(a)-(c), respectively. The results of including all orbits

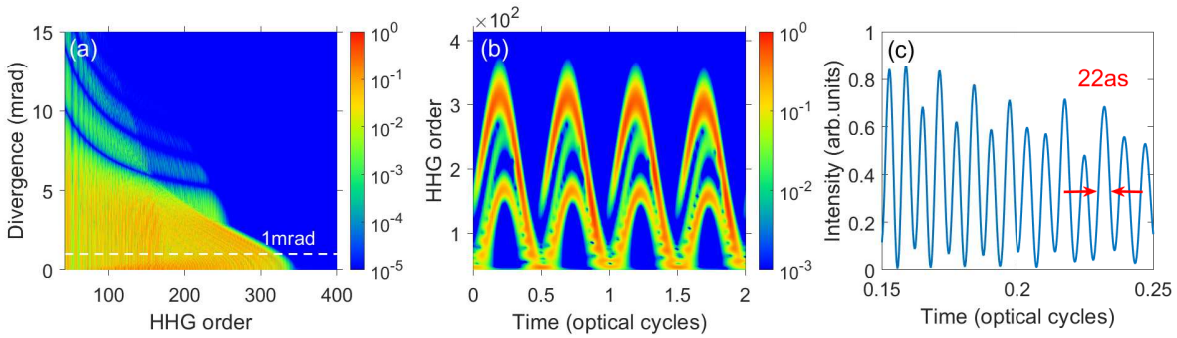


FIG. 10. (a) Intensity profile of the far-field HHG obtained by including all quantum orbits. (b) Time-frequency analysis of the corresponding far-field HHG at 1 mrad. (c) Temporal profiles of attosecond sub-bursts with the duration of 22 as obtained by spectral filtering far-field harmonics at 1 mrad. The driving laser field has the wavelength of 2000 nm with the peak intensity of $1.5 \times 10^{14}$ W/cm$^2$. See text for other simulation parameters.

are shown in Fig. 9(d). One can see that harmonic emissions by the second return orbits are well maintained after the macroscopic propagation, and they are comparable to that by the first return ones. Fig. 9(e) shows the temporal pulses over half optical cycle of the 1600-nm laser. The attosecond sub-bursts with the width of about 33 as appear when the interference between the first return and the second return orbits is included. Further adding the contribution from higher-order return orbits doesn't change the structure of attosecond sub-bursts much. However, attosecond sub-burst is absent when first return or second return orbits are considered individually. In short, the behaviors of attosecond sub-burst waveforms in the macroscopic pulse train are very similar to that in the single-atom response under the conditions of favorable phase matching. Thus to observe attosecond sub-bursts experimentally, it is to use good phase matching by properly adjusting macroscopic parameters and laser focusing condition as illustrated.

In Fig. 10, we show another example with 2000-nm laser using macroscopic parameters in Fig. 7. A 1-mm long gas medium is set at the focus. The far-field harmonic distribution with all quantum orbits included is shown in Fig. 10(a). We select a divergence angle of 1 mrad, as shown by a white line in Fig. 10(a), and the time-frequency picture of the HHG is plotted in Fig. 10(b). The harmonic emissions from the second return orbits are comparable to that from the first return ones. The interference between them leads to attosecond sub-bursts with the duration of about 22 as in the pulse train in Fig. 10(c). These are very close to the attosecond sub-bursts in Fig. 2(d) obtained in the single-atom response. These results are exactly like what we have shown in Fig. 9.

## IV. CONCLUSIONS

In summary, we have shown the existence of attosecond sub-bursts in femtosecond pulse train (FPT) using high harmonics generated by long wavelength lasers. Unlike pulse trains generated by 800-nm lasers where irregular and few sharp bursts appears at each half optical cycle, in the FPTs generated by long wavelength lasers, a large number of regular attosecond sub-bursts appear inside of individual femtosecond pulse profile and each attosecond sub-burst can have duration of few attoseconds, which is scaled by $\lambda_0^{-2}$ with laser wavelength $\lambda_0$. The existence of attosecond sub-bursts has been found to result from the interference of high harmonics due to quantum orbits that undergo first return and second return, with minor corrections from higher returns. These results can be obtained for high harmonics generated from a single atom using the SFA and the QO theories, as well as the QRS model, and the latter has been shown to agree with ab initio calculations from solving the TDSE. To establish that the single-atom predictions can be observed experimentally, we have carried out phase-matching analysis and performed the macroscopic propagation simulations. By simulating the dependence of the single-atom induced dipole phase from individual quantum orbit on the laser intensity by using the classical-trajectory approach, the SFA model, and the TDSE method, the phase coefficients extracted from different methods reach a reasonably good agreement. We showed that the phase coefficient for a given quantum orbit is approximately scaled as $\lambda_0^3$. This has been used to construct the map of coherence length of HHG for each individual quantum orbit and to identify the good phase-matching condition. We have shown that good phase matching of harmonics at small divergence angles can be found for the multiple long quantum orbits if the gas jet is placed at the laser focus. Thus multiple attosecond sub-bursts can occur over half optical cycle of the driving laser in the far-field macroscopic pulse train and maintain the similar pulse width to the single-atom one. Note that if the gas jet is put after laser focus, there would be no attosecond sub-burst structure in the pulse train since only high harmonics due to the "short" orbit in the first return can be well phase matched.

With the advance in the mid-infrared laser, we expect

that shorter-duration sub-burst down to hundreds of zeptoseconds could be generated by spectral filtering high harmonics in a much broader spectral region. This may also be achieved experimentally by controlling the phase matching of different quantum orbits through properly selecting the laser parameters and setting the position of gas medium. This could be realized in two different ways. One way is to increase the intensity of driving laser while the laser wavelength is not increased such that its spatiotemporal waveform is modified upon the propagation in the medium [71, 72]. The effect of free electron cannot be neglected in the analysis of phase matching, so the conditions of reaching the good phase matching for longer quantum orbits need to be adjusted. The other way is to maintain the low laser intensity and then increase the laser wavelength. The theoretical methods may be improved to account for magnetic field [73] and the prediction of this work might have to be modified. While the present study is interesting in predicting new features of FPT generated by long-wavelength lasers, it remains to be seen in experiment. At this time, it is too early to speculate what applications can use such femtosecond pulse trains with attosecond sub-bursts.

## ACKNOWLEDGMENTS

This work was supported by National Natural Science Foundation of China (NSFC) under Grants No. 12274230 and No. 11834004 and Funding of Nanjing University of Science and Technology (NJUST) under Grant No. TSXK2022D005. C.D.L. was supported by Chemical Science Division, Office of Basic Energy Sciences, Office of Science, US Department of Energy under Grant No. DE-FG02-86ER13491. We thank Dr. Hui Wei for useful discussions about the QO model.

[1] A. McPherson, G. Gibson, H. Jara, U. Johann, T. S. Luk, I. A. McIntyre, K. Boyer, and C. K. Rhodes, J. Opt. Soc. Am. B **4**, 595 (1987).
[2] P. Salières, A. L'Huillier, Ph. Antoine, and M. Lewenstein, Adv. At., Mol., Opt. Phys. **41**, 83 (1999).
[3] C. Winterfeldt, C. Spielmann, and G. Gerber, Rev. Mod. Phys. **80**, 117 (2008).
[4] F. Krausz and M. Ivanov, Rev. Mod. Phys. **81**, 163 (2009).
[5] T. Brabec and F. Krausz, Rev. Mod. Phys. **72**, 545 (2000).
[6] L. Y. Peng, W. C. Jiang, J. W. Geng, W. H. Xiong, and Q. Gong, Phys. Rep. **575**, 1 (2015).
[7] T. Popmintchev, M. C. Chen, D. Popmintchev, P. Arpin, S. Brown, S. Ališauskas, G. Andriukaitis, T. Balčiunas, O. D. Mücke, A. Pugzlys, A. Baltuška, B. Shim, S. E. Schrauth, A. Gaeta, C. Hernández-García, L. Plaja, A. Becker, A. Jaron-Becker, M. M. Murnane, and H. C. Kapteyn, Science **336**, 1287 (2012).
[8] J. Seres, E. Seres, A. J. Verhoef, G. Tempea, C. Streli, P. Wobrauschek, V. Yakovlev, A. Scrinzi, C. Spielmann, and F. Krausz, Nature **433**, 596 (2005).
[9] B. Xue, Y. Tamaru, Y. Fu, H. Yuan, P. Lan, O. D. Mücke, A. Suda, K. Midorikawa, and E. J. Takahashi, Ultrafast Sci. **2021**, 9828026 (2021).
[10] P. Ye, L. G. Oldal, T. Csizmadia, Z. Filus, T. Grósz, P. Jójárt, I. Seres, Z. Bengery, B. Gilicze, S. Kahaly, K. Varjú, and B. Major, Ultrafast Sci. **2022**, 9823783 (2022).
[11] P. M. Paul, E. S. Toma, P. Breger, G. Mullot, F. Augé, P. Balcou, H. G. Muller, and P. Agostini, Science **292**, 1689 (2001).
[12] M. Hentschel, R. Kienberger, C. Spielmann, G. A. Reider, N. Milosevic, T. Brabec, P. Corkum, U. Heinzmann, M. Drescher, and F. Krausz, Attosecond metrology, Nature **414**, 509 (2001).
[13] M. Asaki, C. P. Huang, D. Garvey, J. Zhou, H. C. Kapteyn, and M. M. Murnane, Opt. Lett. **18**, 977 (1993).
[14] R. Kienberger, M. Hentschel, M. Uiberacker, Ch. Spielmann, M. Kitzler, A. Scrinzi, M. Wieland, Th. Westerwalbesloh, U. Kleineberg, U. Heinzmann, M. Drescher, and F. Krausz, Science **297**, 1144 (2002).
[15] M. Uiberacker, Th. Uphues, M. Schultze, A. J. Verhoef, V. Yakovlev, M. F. Kling, J. Rauschenberger, N. M. Kabachnik, H. Schröder, M. Lezius, K. L. Kompa, H.-G. Muller, M. J. J. Vrakking, S. Hendel, U. Kleineberg, U. Heinzmann, M. Drescher, and F. Krausz, Nature **446**, 627 (2007).
[16] Y. Huang, J. Zhao, Z. Shu, Y. Zhu, J. Liu, W. Dong, X. Wang, Z. Lü, D. Zhang, J. Yuan, J. Chen, and Z. Zhao, Ultrafast Sci. **2021**, 9837107 (2021).
[17] T. Gaumnitz, A. Jain, Y. Pertot, M. Huppert, I. Jordan, F. Ardana-Lamas, and H. J. Wörner, Opt. Express **25**, 27506 (2017).
[18] J. Li, X. Ren, Y. Yin, K. Zhao, A. Chew, Y. Cheng, E. Cunningham, Y. Wang, S. Hu, Y. Wu, M. Chini, and Z. Chang, Nat. Commun. **8**, 186 (2017).
[19] X. Zhao, S. Wang, W. Yu, H. Wei, Ch. Wei, B. Wang, J. Chen, and C. D. Lin, Phys. Rev. Applied **13**, 034043 (2020).
[20] G. Doumy, J. Wheeler, C. Roedig, R. Chirla, P. Agostini, and L. F. DiMauro, Phys. Rev. Lett. **102**, 093002 (2009).
[21] P. B. Corkum, Phys. Rev. Lett. **71**, 1994 (1993).
[22] K. J. Schafer, B. Yang, L. F. DiMauro and K. C. Kulander, Phys. Rev. Lett. **70**, 1599 (1993).
[23] M. R. Miller, C. Hernández-García, A. Jaroń-Becker, and A. Becker, Phys. Rev. A **90**, 053409 (2014).
[24] L. X. He, Y. Li, Z. Wang, Q. B. Zhang, P. F. Lan, and P. X. Lu, Phys. Rev. A **89**, 053417 (2014).
[25] C. Hernández-García, J. A. Pérez-Hernández, T. Popmintchev, M. M. Murnane, H. C. Kapteyn, A. JarońBecker, A. Becker, and L. Plaja, Phys. Rev. Lett. **111**, 033002 (2013).
[26] J. Tate, T. Auguste, H. G. Muller, P. Salières, P. Agostini, and L. F. Di Mauro, Phys. Rev. Lett. **98**, 013901 (2007).
[27] K. Schiessl, K. L. Ishikawa, E. Persson, and J. Burgdörfer, Phys. Rev. Lett. **99**, 253903 (2007).

[28] K. L. Ishikawa, K. Schiessl, E. Persson, and J. Burgdörfer, Phys. Rev. A **79**, 033411 (2009).

[29] C. Hernández-García and L. Plaja, Phys. Rev. A **93**, 023402 (2016).

[30] D. D. Hickstein, P. Ranitovic, S. Witte, X.-M. Tong, Y. Huismans, P. Arpin, X. B. Zhou, K. E. Keister, C. W. Hogle, B. S. Zhang, C. Y. Ding, P. Johnsson, N. Toshima, M. J. J. Vrakking, M. M. Murnane, and H. C. Kapteyn, Phys. Rev. Lett. **109**, 073004 (2012).

[31] A. Zaïr, M. Holler, A. Guandalini, F. Schapper, J. Biegert, L. Gallmann, and U. Keller, Phys. Rev. Lett. **100**, 143902 (2008).

[32] S. Petrakis, M. Bakarezos, M. Tatarakis, E. P. Benis, and N. A. Papadogiannis, Sci. Rep. **11**, 23882 (2021).

[33] G. Sansone, E. Benedetti, J.-P. Caumes, S. Stagira, C. Vozzi, S. De Silvestri, and M. Nisoli, Phys. Rev. A **73**, 053408 (2006).

[34] L. X. He, P. F. Lan, Q. B. Zhang, C. Y. Zhai, F. Wang, W. J. Shi, and P. X. Lu, Phys. Rev. A **92**, 043403 (2015).

[35] E. J. Takahashi, T. Kanai, K. L. Ishikawa, Y. Nabekawa, and K. Midorikawa, Phys. Rev. Lett. **101**, 253901 (2008).

[36] K. H. Hong, C. J. Lai, J. P. Siqueira, P. Krogen, J. Moses, C. L. Chang, G. J. Stein, L. E. Zapata, and F. X. Kärtner, Opt. Lett. **39**, 3145 (2014).

[37] V. Tosa, H. Kim, I. Kim, and C. H. Nam, Phys. Rev. A **71**, 063807 (2005).

[38] M. B. Gaarde, J. L. Tate, and K. J. Schafer, J. Phys. B **41**, 132001 (2008).

[39] E. Priori G. Cerullo, M. Nisoli, S. Stagira, and S. De Silvestri, Phys. Rev. A **61**, 063801 (2000).

[40] M. Lewenstein, P. Salières, and A. L'Huillier, Phys. Rev. A **52**, 4747 (1995).

[41] M. Lewenstein, Ph. Balcou, M. Yu. Ivanov, A. L'Huillier, and P. B. Corkum, Phys. Rev. A **49**, 2117 (1994).

[42] P. Salières, B. Carré, L. Le Déroff, F. Grasbon, G. G. Paulus, H. Walther, R. Kopold, W. Becker, D. B. Milošević, A. Sanpera, and M. Lewenstein, Science **292**, 902 (2001).

[43] D. B. Milošević and W. Becker, Phys. Rev. A **66**, 063417 (2002).

[44] G. Sansone, C. Vozzi, S. Stagira, and M. Nisoli, Phys. Rev. A **70**, 013411 (2004).

[45] D. J. Hoffmann, C. Hutchison, A. Zaïr, and J. P. Marangos, Phys. Rev. A **89**, 023423 (2014).

[46] A. T. Le, H. Wei, C. Jin, and C. D. Lin, J. Phys. B **49**, 053001 (2016).

[47] T. Morishita, A. T. Le, Z. Chen, and C. D. Lin, Phys. Rev. Lett. **100**, 013903 (2008).

[48] A. T. Le, R. R. Lucchese, S. Tonzani, T. Morishita, and C. D. Lin, Phys. Rev. A **80**, 013401 (2009).

[49] C. D. Lin, A. T. Le, C. Jin, and H. Wei, *Attosecond and Strong-Field Physics: Principles and Applications* (Cambridge University Press, Cambridge, 2018), p. 209-232.

[50] X. M. Tong and C. D. Lin, J. Phys. B **38**, 2593 (2005).

[51] C. Jin, B. C. Li, K. Wang, C. H. Xu, X. Y. Tang, C. Yu, and C. D. Lin, Phys. Rev. A **102**, 033113 (2020).

[52] Z. Guan, Z. M. Yin, and C. Jin, Phys. Rev. A **105**, 023107 (2022).

[53] C. Jin, A. T. Le, and C. D. Lin, Phys. Rev. A **79**, 053413 (2009).

[54] C. Jin, A. T. Le, and C. D. Lin, Phys. Rev. A **83**, 023411 (2011).

[55] J. A. Pérez-Hernández, L. Roso, and L. Plaja, Opt. Express **17**, 9891 (2009).

[56] A. T. Le, H. Wei, C. Jin, V. N. Tuoc, T. Morishita, and C. D. Lin, Phys. Rev. Lett. **113**, 033001 (2014).

[57] P. Ye, X. K. He, H. Teng, M. J. Zhan, S. Y. Zhong, W. Zhang, L. F. Wang, and Z. Y. Wei, Phys. Rev. Lett. **113**, 073601 (2014).

[58] M. Bellini, C. Lyngå, A. Tozzi, M. B. Gaarde, T. W. Hänsch, A. L'Huillier, and C. G. Wahlström, Phys. Rev. Lett. **81**, 297 (1998).

[59] S. R. Abbing, F. Campi, F. S. Sajjadian, N. Lin, P. Smorenburg, and P. M. Kraus, Phys. Rev. Appl. **13**, 054029 (2020).

[60] S. Carlström, J. Preclíková, E. Lorek, E. W. Larsen, C. M. Heyl, D. Paleček, D. Zigmantas, K. J. Schafer, M. B. Gaarde, and J. Mauritsson, New J. Phys. **18**, 123032 (2016).

[61] W. Paufler, B. Böning, and S. Fritzsche, Phys. Rev. A **100**, 013422 (2019).

[62] M. B. Gaarde and K. J. Schafer, Phys. Rev. A **65**, 031406 (2002).

[63] T. Csizmadia, L. G. Oldal, P. Ye, S. Majorosi, P. Tzallas, G. Sansone, V. Tosa, K. Varjú, B. Major, and S. Kahaly, New J. Phys. **23**, 123012 (2021).

[64] T. Auguste and P. Salières, Phys. Rev. A **80**, 033817 (2009).

[65] A. I. Gonzalez, G. Jargot, P. Rigaud, L. Lavenu, F. Guichard, A. Comby, T. Auguste, O. Sublemontier, M. Bougeard, Y. Zaouter, P. Georges, M. Hanna, and T. Ruchon, J. Opt. Soc. Am. B **35**, A6 (2018).

[66] P. Balcou, A. S. Dederichs, M. B. Gaarde, and A. L'Huillier, J. Phys. B **32**, 2973 (1999).

[67] P. Balcou, P. Salières, A. L'Huillier, and M. Lewenstein, Phys. Rev. A **55**, 3204 (1997).

[68] L. E. Chipperfield, P. L. Knight, J. W. G. Tisch, and J. P. Marangos, Opt. Commun. **264**, 494 (2006).

[69] P. Salières, A. L'Huillier, and M. Lewenstein, Phys. Rev. Lett. **74**, 3776 (1995).

[70] C. Hernández-García, J. S. Román, L. Plaja, and A. Picón, New J. Phys. **17**, 093029 (2015).

[71] A. S. Johnson, D. R. Austin, D. A. Wood, C. Brahms, A. Gregory, K. B. Holzner, S. Jarosch, E. W. Larsen, S. Parker, C. S. Strüber, P. Ye, J. W. G. Tisch, J. P. Marangos, Sci. Adv. **4**, eaar3761 (2018).

[72] X. Tang, K. Wang, B. Li, Y. Chen, C. D. Lin, and C. Jin, Opt. Lett. **46**, 5137 (2021).

[73] R. Fischer, M. Lein, and C. H. Keitel, Phys. Rev. Lett. **97**, 143901 (2006).